# Photodissociation dynamics of halogenated aromatic molecules: the case of core-ionized tetrabromothiophene

Lassi Pihlava*[a], Johannes Niskanen[a], Kuno Kooser[b], Christian Stråhlman[c], Sylvain Maclot[d], Antti Kivimäki[e,f] and Edwin Kukk[a]

[a] *Department of Physics and Astronomy, University of Turku, FI-20014 Turku, Finland*

[b] *Institute of Physics, University of Tartu, Wilhelm Ostwaldi 1, EE-50411 Tartu, Estonia*

[c] *Department of Materials Science and Applied Mathematics, Malmö University, SE-20506 Malmö, Sweden*

[d] *Department of Physics, Gothenburg University, Box 100, SE-40530 Gothenburg, Sweden* [e] *MAX IV Laboratory, Lund University, SE-22100 Lund, Sweden*

[f] *Nano and Molecular Systems Research Unit, University of Oulu, Fi-90570, Oulu,Finland*

* *corresponding author, leapih@utu.fi*

## 1 Introduction

Photoresponse of halogenated organic molecules has been actively studied in recent years, in particular in the realm of multiphoton x-ray absorption and following femtosecond-scale photodynamics in real time at the free electron laser light sources.[1–14] However, the data and understanding of the photodissociation patterns and dynamics, following fundamental single-photon core ionization of halogenated and especially fully halogenated organic compounds, is scarce. Here, we investigate the photodissociation induced by soft x-ray absorption in tetrabromothio phene molecule ($C_4Br_4S$), comprised of a thiophene ring and four bromine atoms, each attached to a carbon site. Henceforth, we will refer to the intact thiophene ring by R and its fragments generally as $R_f$ (using this convention $C_4Br_4S$ becomes $Br_4R$).

Tetrabromothiophene is an interesting target for several reasons. First, it is a planar molecule, whose light-atom ring structure is surrounded by heavy bromine atoms. Under multiphoton ionization conditions, this creates a "Coulomb implosion" effect in the photodissociation[13]. It remains an open question how this "inertial cage" affects the dissociation following a single coreionization event. Second, lack of hydrogens means that the dissociation will not include fast isomerization related to ultrafast hydrogen dynamics. Thus, the possible intermediate geometries along the dissociation pathways are likely more straightforwardly linked to the ground state geometry. Third, the heavy elements act as absorption hotspots for high-energy photons, significant for example in the action of certain radiosensitizers in radiotherapy.[7,15–17]

In the present study, we used synchrotron radiation combined with energy-resolved electron-ion multiparticle coincidence spectroscopy. Tunable and monochromatic synchrotron radiation is optimal for core ionization targeted at specific atomic sites and orbitals as the first step of the photodynamics. In this paper we will not make a further distinction between core and inner shell electrons, but denote orbitals either core or valence (V). Electronenergy-resolved coincidence measurements allow us to (i) link the observed fragmentation pattern firmly to a specific photoionization process or (ii) to study the dependence of the fragmentation pattern on the dicationic electronic state. Such a combined state (energy) and site specific investigation sheds light onto the mechanisms of fragmentation and the ways to steer the process. The experiment also allows us to assess some common concepts of molecular photodissociation *e.g.* the role of rapid internal conversion into the dicationic ground state as the main driving factor in morphing the fragmentation dynamics.

We studied $Br_4R$ upon core-ionization events (Br 3*d*, C 1*s* and S 2*p*) that create rapidly dissociating dicationic states via Auger decay. Additionally, as a reference we have measurements with valence and Br 3*p* ionization, which produced singly charged and tricationic states, respectively. In section 3 we examine the dissociation following the Br 3*d* ionization in detail and propose a generalized description of the occuring molecular dynamics – a "dissociation tree". We used coincident measurements of ions with Auger electrons to investigate dissociation rates as a function of the available internal energy of the parent dication. Next, in section 4 we study the core-hole-site dependence of the fragmentation process. We compare

the observations with first-principles theoretical predictions on dicationic electronic state populations and on the effects of core-ionized nuclear dynamics.

## 2 Experiment

All experiments were performed at the Finnish-Estonian soft Xray beamline (FinEstBeams) of MAX IV synchrotron radiation facility in Lund, Sweden. The beamline[18] is equipped with a SX700 type plane grating monochromator (FMB Feinwerk-und Messtechnik GmbH), receiving radiation from an Apple II type undulator. Tetrabromothiophene sample (Sigma-Aldrich, 99% purity) was introduced into the Gas-phase Endstation (GPES)[19] from an in-vacuum crucible. In order to limit the evaporated sample flow, the sample was cooled down to approximately 13 °C using a water-cooling system. The gas pressure in vacuum chamber was about 1.1-1.7 x $10^{-6}$ mbar during experiments. The molecular jet from the capillary crossed the monochromatized photon beam at the centre of the sample region (Fig. 1), and the ejected electrons were detected by a modified Scienta R4000 hemispherical electron analyzer, equipped with a fast 40 mm diameter microchannel plate (MCP) and resistive anode (Quantar Inc.) position sensitive detector. Detected electrons were used as triggers for the pulsed ion extraction voltage $U_S$ across the source region of a modified Wiley-McLaren type ion time-of-flight (TOF) spectrometer[20]. The ions were then accelerated to the final energy by the drift tube voltage $U_A$, first passing a lens element with $U_L$ that modified their radial distribution and focusing. Ions were detected by a Roentdek 80 mm MCP and HEX-anode detector, recording ion flight times and radial hit positions. The used photon energies were 25 eV for valence ionization, 100 and 150 eV for Br 3*d*, 180 eV for S 2*p*, 260 eV for Br 3*p* and 320 eV for C 1*s*.

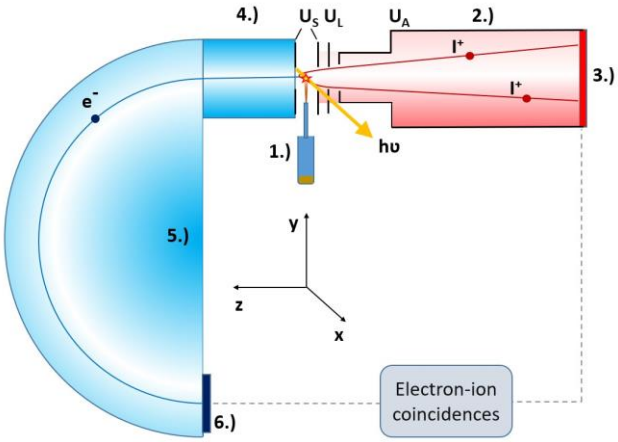


Fig. 1. Schematics of the electron-ion coincidence experiment at the Gasphase Endstation. The labeled main components: 1.) sample crucible and inlet, 2.) ion TOF spectrometer, 3.) ion detector, 4.) electron lens, 5.) electron analyzer and 6.) electron detector.

In a coincident experiment multiple particles originating from a single molecule are detected, which enables determining interdependencies between their properties. Specifically, we have employed electron-photoion-photoion coincident (PEPIPICO) spectroscopy, where the detection of an electron acts as a starting trigger for the time-of-flight measurement. Electrons were either photoelectrons or Auger electrons, depending on the measurement. The measured electron energy and ion TOF and position data were combined into a coincidence dataset.

Alongside with the electron triggers we also used noncoincident "random" triggers for ion extraction. The random triggers were obtained from a pulse generator at a constant rate. The recorded events after electron triggers are a mixture of true and false coincidences while the events related to random trigger can be thought of as purely false coincidences. Thus, the ions collected using random triggers can be utilised for statistical subtraction of the false coincidence background. The procedure is explained in detail elsewhere[21].

The electron energy window for a coincidence dataset is determined by the electron acceleration/retardation and the pass energy $E_p$ of the analyzer, its width being about 8% of $E_p$. For different electron energy resolution/energy coverage optimization, data with $E_p$=50, 100 and 200 eV were recorded, with the entrance slit of the spectrometer at 0.8 mm (for $E_p$=200 eV), 2.5 mm ($E_p$=50 and 200 eV) or 4.0 mm ($E_p$=100 and 200 eV), giving the estimated electron energy resolution of 400, 100, 1250, 1000 and 2000 meV full-width at half-maximum (FWHM), respectively. The used settings were chosen depending on the studied feature.

Ion extraction and acceleration voltages marked in Fig. 1 were $U_A$ = −1830 V, $U_L$ = −300 V and $U_S$ = ±300 V.

## 3 Dissociation pathways following Br 3*d* photoionization

We have used various complementary analyzing methods to build a complete picture of dissociation processes upon Br 3*d* ionization. This neutral Br atoms. The ring does occasionally break but the fragmentation pathways resulting in the $BrR_f^+$ ions

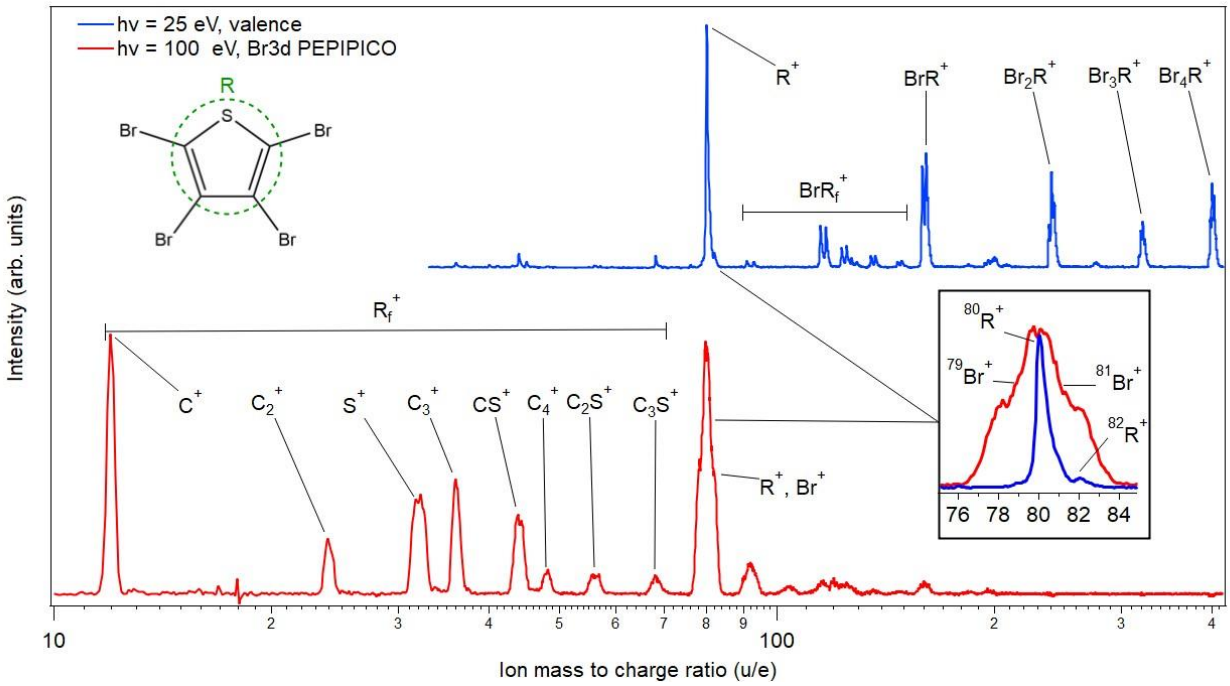


Fig. 2. Ion mass spectra with valence ionization (blue) and from Br 3*d* PEPIPICO measurement (red) on logarithmic scale. The contribution of false coincidences has been removed. The left side of the valence TOF is cropped out due to contribution of the rest gas and lack of peaks from the sample. The feature at $m/z \approx 80$ u/e is much broader in the Br 3*d* measurement than in the case of valence ionization due to presence of $Br^+$ ions (inset).

also likely include neutral Br loss. If these fragments were produced strictly by two body dissociation, we would expect to see similar traces of $Br_3R^+_f$ fragments, which are now nearly absent, unless the charge always remains with the lighter fragment. After coreionization the ring fragmentation becomes much more relevant and the weight of the TOF spectrum overall shifts towards light $R^+_f$ ions ($m/z < 80$ u/e).

Ionic fragments can be identified in a TOF spectrum since the flight time of an ion is proportional to the square root of its mass to charge ratio. Fragments with similar flight times may overlap one another in the spectrum and these spectral structures cannot always be is done to ensure better readability. First, time-of-flight spectrometry allows us to identify the released ionic fragments. Second, with ion-ion coincidence (PIPICO) data we can link detected cations to a single ion pair and deduce what neutral fragments could be involved in dissociation. This way we may already propose possible fragmentation pathways for some ion pairs. Finally, we consider internal-energy dependence of ion production by studying Auger electron kinetic energy by using the PEPIPICO method. Within the framework of statistical thermodynamics and rapid internal conversion, internal energy is the deciding attribute for the dissociation outcome.

### 3.1 Identification of ionic fragments

We present TOF spectra following the ionization of valence (blue spectrum) and Br 3*d* electrons (red spectrum) in Fig. 2. In the case of valence ionization, $Br_4R$ dissociates predominantly by shedding neutral Br atoms. The ring does occasionally break but the fragmentation pathways resulting in the $BrR_f^+$ ions also likely include neutral Br loss. If these fragments were produced strictly by two body dissociation, we would expect to see similar traces of $Br_3R^+_f$ fragments, which are now nearly absent, unless the charge always remains with the lighter fragment. After coreionization the ring fragmentation becomes much more relevant and the weight of the TOF spectrum overall shifts towards light $R^+_f$ ions ($m/z < 80$ u/e).

Ionic fragments can be identified in a TOF spectrum since the flight time of an ion is proportional to the square root of its mass to charge ratio. Fragments with similar flight times may overlap one another in the spectrum and these spectral structures cannot always be decomposed by resolution alone. In $Br_4R$ this overlap is observed most notably in structure at

$m/z \approx$ 80 u/e, which may corresponds to $Br^+$ ($^{79}Br$ and $^{81}Br$ isotopes in 1:1 ratio), $R^+$ (80 u/e) and dication $BrR^{++}$ (79.5 u/e and 80.5 u/e).

The structures at $m/z \approx$ 80 u/e are shown closely in the small inset panel of Fig. 2. The blue spectrum does not contain $Br^+$ notably as the two bromine isotopes would cause broadening in the sharp peak profile. Additionally, a small adjacent peak from the heavier sulfur isotope ($^{34}S$) is clearly visible in the correct ratio. The presence of dications cannot be confirmed here but their creation is thought to be unlikely with valence ionization.

The corresponding analysis is much more difficult in the case of Br 3*d* since the peak is rather broad. Overall, the red lineshape could be formed by including only $Br^+$ ions or a combination of $Br^+$ and $R^+$. The lineshapes of individual bromine isotopes are broad due to kinetic energy release in dissociation and structure could reach its maximum at $m/z$ = 80 u/e as a simple result of superposition. $Br^+$ originating from different dissociation pathways may also produce different lineshapes. Alternatively, the $R^+$ ion could just as well be located between the bromine isotopes resulting in a identical lineshape. There is no reason to assume that all $R^+$ ions would fragment further into $R^+_f$. However, the actual ratio of $Br^+$ and $R^+$ will remain unknown for now.

One way to separate overlapping cationic and dicationic fragments is to look at the ion hit position (distance from the spectrometer's central axis) as a function of flight time. When a dication dissociates, a released cation pair gain more kinetic energy due to Coulombic repulsion than a pair consisting of a dication and a neutral fragment. Cations released perpendicularly against the central axis are detected at a time $T$ at some distance $r$ from the axis. Cations initially moving towards or away from the detector remain on the axis but are detected at times $T \pm \Delta T$. Dications with flight time $T$ on the other hand stay close to the axis regardless of the initial moving direction. By filtering based on the hit position and flight times we can isolate dications from cations to a certain degree. This method is used later in section 3.3.

### 3.2 Analysis of the PIPICO data

Coincident ion pairs from the three-particle PEPIPICO measurement following Br 3*d* ionization are presented in a PIPICO map in Fig. 3. The flight times of an ion pair are plotted against each other, with the faster ion on x-axis and the slower one on y-axis. We will accordingly refer to ion pairs with notation (faster ion, slower ion). Thus, a single dissociation event forms a single dot on the map. All identical ion pairs do not fall exactly on the same spot on the map but they form patterns. For visualization, the map is divided into 2D bins with color portraying the number of dots.

With ion pair analysis we can study individual PIPICO patterns and determine how many ion pairs (per trigger) we have detected there. This way we can estimate *e.g.* what portion of all $R^+_f$ ions are coincident with other $R^+_f$ ions. As stated earlier, the removal of random ion background relies on averages and this is naturally reflected in the ion pair analysis. Additionally, all ions cannot be detected near the diagonal of the map due to dead time effects and the number of detected ions per trigger will be underestimated there. Nevertheless, pair analysis will serve us as a valuable guide.

The PIPICO map in Fig. 3 is strongly characterized by ion pairs, which contain at least one ion with $m/z \approx$ 80 u/e (approx. 8900 ns). Based on the previous section, the coincidence can correspond to either $Br^+$, $R^+$ or dication $BrR^{++}$. However, now the total charge of the parent molecule is +2 and consequently the dication cannot be present in a true coincident ion pair.

We have divided notable PIPICO patterns into nine areas based on their contents. Areas I-IV contain of the aforementioned ion pairs containing at least one $Br^+$ or $R^+$ and these areas contribute approximately 82 % of all true coincident ion pairs. More precisely, 43 % of all true coincident ion pairs are in area I, 18 % in area II, 15% in area III and 5.8 % in area IV. Patterns in area I consist of ring fragments $R^+_f$, which must be coincident with a bromine ion. Both ions in the pattern of area II have $m/z \approx$80u/e, which means that possible ion pairs are $Br^+$+$Br^+$ and $Br^+$+$R^+$. The slower ion in area III is $BrR_f^+$, meaning that ring ion cannot be present. Area IV has a bromine ion in coincidence with $BrR^+$ or $R^+$ with $Br^+_2$. Ion pairs of areas V-IX are easy to identify due to lack of TOF overlap and they are simply marked in Fig. 3. Area V contributes 6.3 % of all ion pairs, area VI contributes 8.0 % and the remaining 4 % belong to areas VII, VIII and IX. Overall, the intact ring $R^+$ can only be detected in areas II, IV and IX as all other patterns require ring breakage.

Due to conservation of momentum, the velocities of dissociation products will be correlated and the slope $k$ of a PIPICO pattern will depend on the taken fragmentation pathway. Slope analysis is challenging when a pattern is weak or when it has merged with its neighbour. Patterns belonging to different Br iso topes overlap and have slightly different slopes because of different masses. Hence, we will mostly apply slope analysis to area I, which contains the strongest patterns besides area II. Because of the two isotopes, the experimental slopes have been estimated by drawing two lines inside each pattern and measuring the slope of those lines (see Fig. 4). The method is not exact and the slope error generally increases as the slope deviates from -1. As such, our slope analysis cannot be used to directly validate individual dissociation pathways but rather to rule out ones that are clearly contradictory.

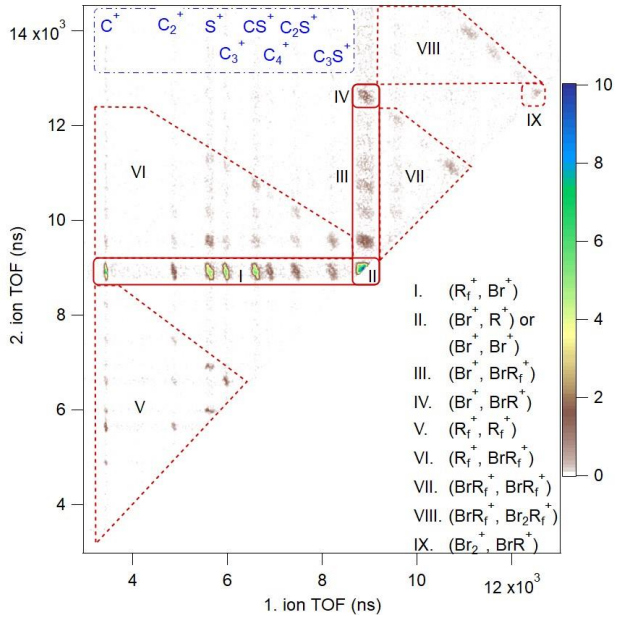


Fig. 3. Br 3*d* photoelectron PIPICO map with false coincidence background removed. Areas with notable patterns are highlighted in red. Areas with solid highlight (I-IV) contain the strongest patterns based on ion pair analysis while dashed areas (V-IX) belong to less important branches of the main dissociation tree. The blue labels mark vertical regions corresponding to the named ring fragment $R_f^+$.

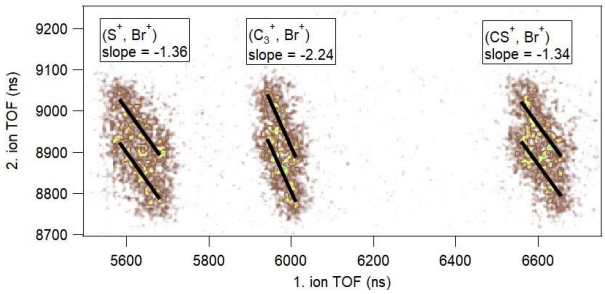


Fig. 4. The region of the PEPIPICO map with the strongest ($R_f^+$, $Br^+$) patterns in area I of Fig. 3 excluding ($C^+$, $Br^+$). The patterns for ($S^+$, $Br^+$), ($C^+_3$, $Br^+$) and ($CS^+$, $Br^+$) are marked with two black lines due to two bromine isotopes. The slopes of the lines are marked above. A smaller 2D bin size was used than in Fig. 3.

By assuming that kinetic energy is released mostly when the charges separate, we can calculate theoretical slopes for different pathways. Patterns in area I seem to mainly correspond to deferred charge separation followed by secondary dissociation, where the lighter ion ($R_f^+$) is released in the final step. Generally, such a process for a dication $ABCD^{++}$ releasing two cations ($B^+$, $C^+$) is written as

$ABCD^{++} \rightarrow ABC^{++} + D \rightarrow AB^+ + C^+ + D \rightarrow A + B^+ + C^+ + D$,

which corresponds to slope equation

$$k \approx -M(AB^+)/M(B+) . \qquad (1)$$

Therefore, the slope of ($B^+$, $C^+$) pattern depends on the mass ratio of precursor $AB^+$ and cation $B^+$ while the mass of cation $C^+$ does not affect the slope. Out of the eight patterns of group I, all but ($S^+$, $Br^+$) and ($CS^+$, $Br^+$) have slopes corresponding to the pathway

$Br_4R^{++} \rightarrow 3\ Br + BrR^{++} \rightarrow 3\ Br + Br^+ + R^+$

$$\rightarrow 3\ \mathrm{Br} + \mathrm{Br}^+ + (\mathrm{R_f^+} + \mathrm{R_f}).$$

Here $R_f^+$ and $R^+$ correspond respectively to $B^+$ and $AB^+$ of the general slope equation 1. With ($S^+$, $Br^+$) and ($CS^+$, $Br^+$) the preceding case results in slopes -2.5 and -1.82, respectively. The experimental slopes on the other hand are approximately -1.4 in both cases.

For ($S^+$, $Br^+$) a more suitable dissociation pathway would be

$$Br_4R^{++} \rightarrow Br_3C_3 + BrCS^{++} \rightarrow Br_3C_3 + Br^+ + CS^+$$

$$\rightarrow Br_3C_3 + Br^+ + (C + S^+),$$

for which equation 1 is still valid. Using $S^+$ and $CS^+$ as $B^+$ and $AB^+$ we end up with slope -1.38 that is reasonably close to the experimental value.

For ($CS^+$, $Br^+$) we propose a pathway, where after deferred charge separation both cations undergo secondary dissociation:

$$Br_4R^{++} \rightarrow 3\ Br + BrR^{++} \rightarrow 3\ Br + BrC^+ + C_3S^+$$

$$\rightarrow 3\ Br + (C + Br^+) + (C_2 + CS^+)$$

which corresponds to slope equation

$$k \approx -M(Br^+)\, M(C\ S^+)/M(CS^+)\, M(BrC_3^+). \qquad (2)$$

This pathway leads to slope of -1.34, which is quite close to the estimated value. All estimated slope values and the final calculated slopes are presented in table 1.

Interestingly, ($C^+$, $Br^+$) ions are not produced noticeably in the same pathway as ($CS^+$, $Br^+$) as the experimental slope is too steep, even though the pathway does include neutral C. Also, ($CS^+$, $Br^+$) is an intermediate stage in a pathway leading to ($S^+$, $Br^+$) but detected ($CS^+$, $Br^+$) pairs must originate from a different dissociation process to match the slope.

The above correlation analysis of the PIPICO patterns assumes a distinct step-wise dissociation model, which has frequently proven suitable for the dissociation of molecules comprised of light atoms.[2,22,23] Here, the model suggests separa tion of bromine and Br-containing neutral fragments in the initial stage, which then has little or no momentum exchange with the remaining dicationic part of the molecule. Considering the geometry of the molecule and slow separation of the heavy neutral fragments, it is in fact somewhat surprising that reasonable deferred charge separation pathways could be found in the stepwise model, with very good agreement with the observed PIPICO patterns in Fig. 3.

Table 1. Estimated and calculated slopes for ($X^+$, $Br^+$) patterns in area I.

| **Ion X** | **$C^+$** | **$C_2^+$** | **$S^+$** | **$C_3^+$** | **$CS^+$** | **$C_4^+$** | **$C_2S^+$** | **$C_3S^+$** |
|---|---|---|---|---|---|---|---|---|
| **Est.** | -6.6 | -3.3 | -1.4 | -2.2 | -1.4 | -1.6 | -1.4 | -1.2 |
| **Calc.** | -6.66 | -3.33 | -1.38 | -2.22 | -1.34 | -1.66 | -1.43 | -1.17 |

### 3.3 Energy dependency of ion yields and the proposed dissociation tree

Here, kinetic energy of an Auger electron can be linked to internal energy of the dicationic parent:

$$E_{int}(M^{++}) = E_b - E_{kin} - V_{DIP}, \qquad (3)$$

where $E_b$ is the binding energy of the core electron. The double ionization potential $V_{DIP}$ is included to calibrate the energy scale with respect to the dicationic ground state. In a coincident measurement, the above relation can be used to determine appearance energies (AEs) of different fragments (*i.e.* minimum internal energy after which the fragment is produced). This allows us to gain insight into the dissociation energetics.

PIPICO maps such as Fig. 3 cannot reveal a possibly important aspect of the photodynamics following the population of dicationic states – the production of undissociated parent $Br_4R^{++}$ and dicationic fragments if charge separation does not occur in dissociation. Fig. 5 shows the coincident ions yields (CIYs) of detected dications as a function of the kinetic energy of the coincident Br 3*d* Auger electron.

Although the dications form a minor fraction of the total ion yields, they provide important clues in reconstructing the prevailing dissociation sequences – that we will refer to as the dissociation tree. Their AEs also allow us to determine various internal energy thresholds early in the tree model.

In order to have a systematic procedure for the determination of the AEs of dications as well as cations analyzed later, we used least-squares Gaussian fits on the rising edges of the ion yields (see Figs. 5 and 6). The AE was estimated as the energy at which the tangent line from the half-maximum point of the Gaussian fit curve intercepts the constant background level of the fit. The doubly charged parent appears at $E_{kin}$ = 55.4 eV. We measured the binding energies of Br $3d_{5/2}$ and Br $3d_{3/2}$ electrons in $Br_4R$ to be 76.7 eV and 77.7 eV, respectively. Thus, according to eqn (3), $V_{DIP}$ is 22.3 eV. All AEs are listed in table 2

Due to spin-orbit splitting there are in fact two initial corehole states with populations in 3:2 ratio. As a consequence, all CIY curves plotted against Auger $E_{kin}$ have two components, one stemming from Br $3d_{5/2}$ ionization and the other from Br $3d_{3/2}$. The only differences between the curves is that their intensities

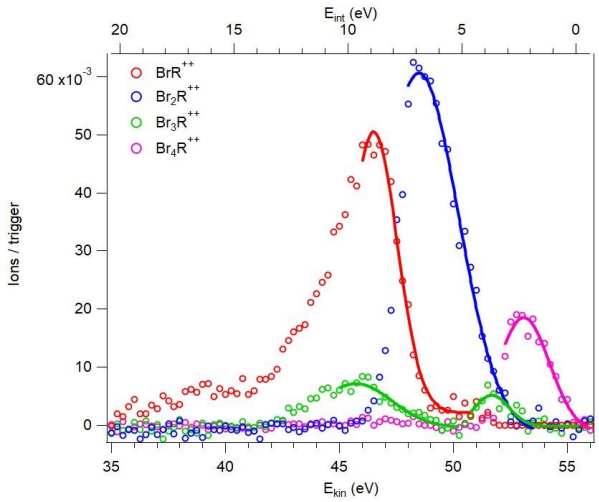


Fig. 5. CIYs of doubly charged ions as a function of the kinetic energy of the Br $M_{4,5}V^{-2}$ Auger electron. False coincidence background has been subtracted using random-triggered events. The fitted Gaussians (solid lines) are used to determine appearance energies of each dication and the appearance of doubly charged parent marks the zero of internal energy (top axis) as stated in eqn (3).

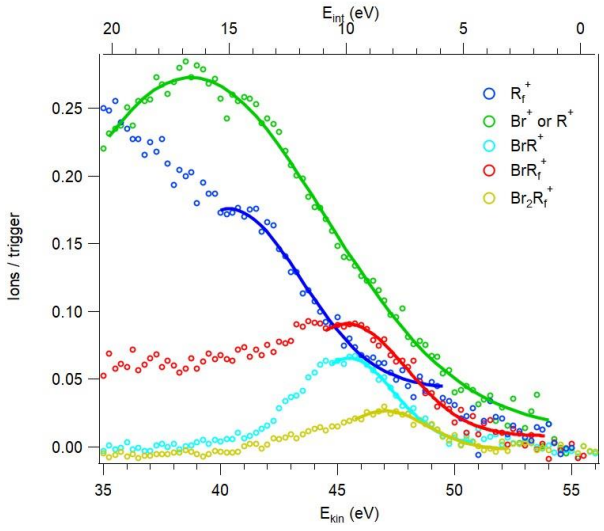


Fig. 6. CIYs of cation groups as a function of the kinetic energy of Br $M_{4,5}NN$ Auger electron after subtraction of the false coincidence background and the ion yield from processes other than the Br $M_{4,5}V^{-2}$ Auger decay. The fitted Gaussians (solid lines) are used to determine

appearance energies of each group. Due to presence of unwanted background, only the steeply rising part of $R_f^+$ CIY is fitted, which leads to high base level for the Gaussian.

Table 2. AEs for cation species and dications in terms of internal energy.

| Dication | $Br_4R^{++}$ | $Br_3R^{++}$ | $Br_2R^{++}$ | $BrR^{++}$ | |
|---|---|---|---|---|---|
| AE (eV) | 0.0 ± 0.3 | 2.2 ± 0.4 | 3.4 ± 0.4 | 6.8 ± 0.3 | |
| Cation | $Br_2R_f^+$ | $BrR^+$ | $BrR_f^+$ | $Br^+$ ($R^+$) | $R_f^+$ |
| AE (eV) | 4.7 ± 0.5 | 6.0 ± 0.4 | 4.9 ± 0.4 | 4.8 ± 0.4 | 8.8 ± 0.5 |

are weighted by their related populations and the other one is shifted in Auger $E_{kin}$ by the amount of spin orbit splitting, now approximately 1.0 eV. Therefore, the zero of internal energy in the graphs is vis-à-vis Br $3d_{3/2}$, while the dicationic parent from

Br $3d_{5/2}$ appears at $E_{kin}$ = 54.34 eV. It should be noted that the double ionization potential is not affected by the splitting.

Valence ionization was characterized by neutral Br loss. In Fig. 5 we can observe the same dynamics and its energy dependence with dications. The first neutral Br ejection appears at $E_{int}$ = 2.2 eV and the second quickly afterwards at 3.4 eV. The lineshape of $Br_3R^{++}$ is clearly composed of two separate peaks and the peak at higher internal energy extends over the same energy range as $BrR^{++}$. This is highly suspicious considering the apparent Br loss dynamics, *ergo* the higher internal energy peak most likely belongs to some other fragment. The most probable candidate is $BrR^+$, which has the same mass to charge ratio and a similar energy range in Fig. 6. Due to flightime overlaps, dications were filtered from the cations based on their hit position on the detector. There were no clear-cut threshold values for filtering, which is why some $BrR^+$ ions passed through the process. Additionally, the true $Br_3R^{++}$ peak is rather small and noisy, making accurate determination of its AE challenging. We suspect that the energy gap between the one and two neutral Br loss channels is a bit smaller than the one given by our method, which likely explains the lack of detected $Br_3R^{++}$. With only a little extra energy the second Br loss channel becomes available and the apparent strong tendency to lose neutral Br makes the new channel dominant. The ejection of the third Br requires considerably more energy than the previous two with AE of 6.8 eV. As such, the $Br_2R^{++}$ and $BrR^{++}$ channels are clearly separated from one another. We did not observe $R^{++}$ with Br 3*d*.

As noted in earlier, random background removal is challenging with ion pairs. With single ions (TOF instead of PIPICO), the process becomes much more straightforward and reliable. Therefore, all ion yields presented here are single ion yields. This means that the single ion yield curves get contributions from all possible dissociation pathways. Instead of studying every ion by itself, we have decided to study broader fragment groups presented in Fig. 3. From the coincident ion pair analysis we know that 82 % of ion pairs were in areas I-IV and out of all $R^+_f$ ions 75 % were in area I. Consequently, we can deduce that the single ion yield of $R^+_f$ is mostly related to dissociation pathways leading to area I.

As can be seen from the Auger electron spectrum (Fig. 7), the Auger intensity in the region above 48 eV is quite low. At the same time, there is a significant background of electrons from other sources, such as secondary emission from surfaces inside the spectrometer partially exposed to synchrotron light, or Auger processes following deeper core ionization by higher-order light. The processes of the latter type contaminate the coincident data, as singly charged ions from such processes are detected as well. The $R_f^+$, $Br^+$ or $R^+$, and $BrR_f^+$ ion yields in particular fall to a nonzero background level even at the electron energies above $V_{DIP}$. There was no such background contribution to the doubly charged ions. We used these background values above $V_{DIP}$ to subtract the contribution to the cation yields that is not related to the Br 3*d* Auger decay process.

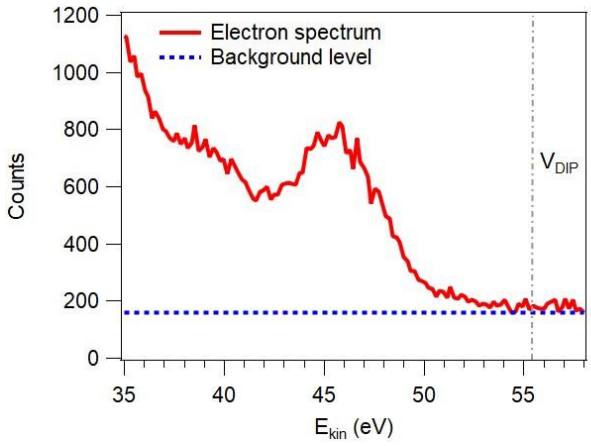


Fig. 7. Br $M_{4,5}V^{-2}$ Auger spectrum. The dashed horizontal line shows the approximate background level due to unwanted secondary electrons and the vertical dashed line shows the location of $V_{DIP}$.

The $R_f^+$ ion yield in Fig. 6 is an especially challenging one to fit. Since the yield does not start to lower or even plateau at high internal energy and the background contribution is not constant, the Gaussian fit approach is not very well suited for its case. Therefore, we have opted to fit only the part with the steepest incline even though the the Gaussian base level is too high. If the fitted energy range were larger, the quality of the fit would visibly decrease. Distinguishing between cations due to background and "true" pathways is not possible but we attribute the notable, steep incline to an important fragmentation pathway opening. By choosing to fit it accurately, we will get a rough estimate of its AE. Additionally, the $R_f^+$ ion yield likely corresponds to multiple dissociation channels, which all have their own AEs.

Based on the slope analysis and the CIY curves, we propose that dissociation of doubly charged tetrabromothiophene mainly follows pathways presented in Fig. 8. Generally speaking, no ion pair is a product of a simple two-body dissociation of the dicationic parent; each visible PIPICO pattern in Fig. 3 implies some neutral fragments. The heaviest detected ion pairs (in areas VIII and IX) are missing a neutral Br when compared to the parent while ion pairs in areas IV and VII are missing a minimum of two neutral Br atoms. Additionally, because the ejection of one or two neutral Br atoms requires less internal than any other process, dissociation likely often starts with the Br ejection. Therefore, $Br_4R^{++}$ mainly dissociates via deferred charge separation, which may continue with secondary dissociation.

The presence of dications supports the proposed dissociation tree. All detected dications except the parent only involve neutral Br ejection and the possible subsequent ion pairs appear at higher internal energies than the dication preceding them. Ion pair analysis of area I on the other hand at towards neutral Br loss prior to charge separation and ring fragmentation. Even though most detected ions are cations (as can be seen in the Br 3*d* TOF of Fig. 2), the dications are important intermediate stages, which can be thought to form the "trunk" of the dissociation tree.

The CIYs of cation groups (Fig. 6) and the number of Br atoms in the ions allow us to estimate the dissociation tree's branches. $Br_2R_f^+$, $BrR_f^+$ and $Br^+$ all appear nearly simultaneously between 4.7 eV and 4.9 eV, meaning that they all can be reached from either $Br_3R^{++}$ or $Br_2R^{++}$. Naturally, ion pairs containing 3 Br atoms can only originate from the former. Quite interestingly $BrR^+$ of area IV appears at 6.0 eV, over 1 eV higher than first pathways requiring ring fragmentation. Finally, $R_f^+$ ions appear at 8.8 eV placing them at the top of the dissociation tree.

Ion pairs in the important area I required dications as precursors and consequently heavier ion pairs cannot be intermediate products in pathways resulting in ($R_f^+$, $Br^+$) ion pairs. Dissociation channels leading to area I must then branch off directly from the dication "trunk" of the dissociation tree.

As stated in the slope analysis section, seven of the eight ion pairs in area I branch of directly from $BrR^{++}$. In six pathways the dication undergoes charge separation into $Br^+$ and $R^+$. The ring structure then subsequently breaks down into $R_f^+$ and neutral $R_f$. In Fig. 8 pathway resulting in ($CS^+$, $Br^+$) is included in the same pathway arrow but the ring fragmentation is already a part of the charge separation as $BrR^{++}$ splits into $BrC^+$ and $C_3S^+$. The remaining Br atom rips the ring structure open and takes a carbon atom with it. In order to form the ion pair both fragments need to undergo secondary dissociation.

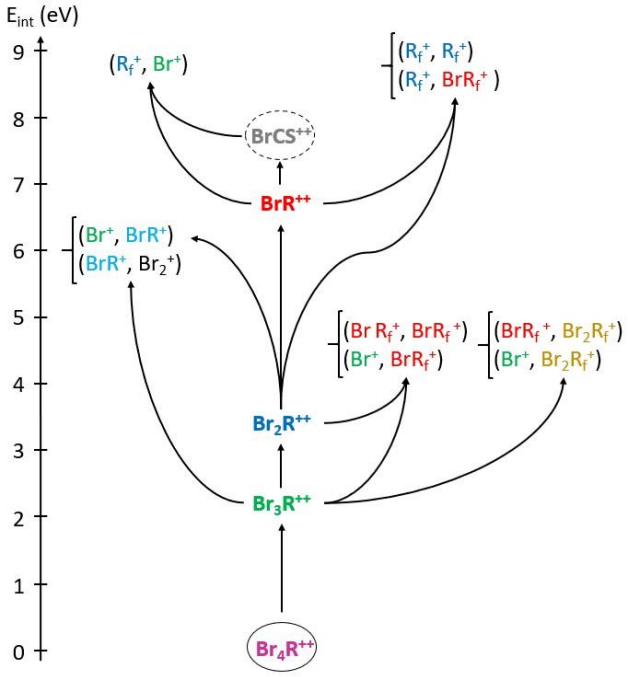


Fig. 8. Proposed general main dissociation tree for the doubly charged parent molecule. All neutral fragments are omitted, and the colors refer to Fig. 5 and 6. Dications and cation pairs are placed at their appearance energies (determined from Fig.5 and 6) and the arrows indicate the main dissociation pathways. Several minor dissociation pathways are not shown. The existence of the intermediary product $BrCS^{++}$ was deduced from the slope analysis of the PIPICO data.

($S^+$, $Br^+$) is an outlier in area I as its dissociation undergoes a bit differently. According to the slope analysis precursor to the ion pair is $BrCS^{++}$, which breaks down to $Br^+$ and $CS^+$, and further to C and $S^+$. The entire process would start with ejection of neutral three neutral bromine atoms and three carbon atoms. Slope analysis cannot tell us whether the neutral atoms are ejected one by one or as a single fragment before charge separation, but a more feasible alternative might be ejection of $Br_3C_3$ as it requires least bond breakages. The dication $BrCS^{++}$ was not detected at all, which also means that we cannot establish its appearance energy and place it accurately in the dissociation tree. If the elusive dication is indeed formed in the presented pathway, it must be quite unstable.

Pathways leading to ($Br^+$, $Br^+$) and ($Br^+$, $R^+$), *i.e.* area II, cannot unfortunately be placed into the tree. Since $Br^+$ is produced in various pathways, its CIY peak in Fig. 6 is very broad and there is no way to distinguish between individual channels. In a similar manner, the CIY curve of $R_f^+$ is also very broad and it does not come down as internal energy increases. This behaviour is due to the fact that $R_f^+$ and $Br^+$ are ultimate products as they cannot be broken down any further into some other ion group.

The earlier study[24] on dissociation of doubly charged thiophene $H_4R^{++}$ shares similarities with our current study. First, the neutral hydrogen loss in thiophene was observed to be important. However, the ejection of neutral side atoms in thiophene occurs as a secondary process after ring opening and fragmentation in the dominant channels. The neutral side atom loss is also a strongly energy dependent process and the appearance energies for the first and second loss are bundled together. Despite this, the channel with first hydrogen loss remains dominant over the second loss channel over a large internal energy range unlike in $Br_4R$. The hydrogen loss requires more energy than removal of bromine. Light hydrogen atoms likely adapt more easily to changes in the ring geometry while heavy bromine atoms hinder the adjustments with their great mass (ratio of ring mass to side atom masses is 20:1 in thiophene and 1:4 in tetrabromothiophene). If the ring structure is to change, ring atoms must push/drag around the bromine atoms, which causes the ring fragmentation to occur at higher internal energies than in thiophene and neutral Br loss becomes the preferred first step. Consequently, ring fragmentation in tetrabromothiophene requires more energy than in thiophene. This is also supported by the valence ionization TOF spectrum, which was characterised by the prevalence of neutral Br loss.

# 4 Effect of the core-ionization site on the dissociation

## 4.1 Experimental ion yields

Like with Br 3*d* ionization, the system undergoes Auger decay into some dicationic states after ionizing C 1*s* and S 2*p*. Regardless of the ionization site and different binding energies, the resulting two holes will be in the valence and the $V_{DIP}$ will be the same in all three cases. Since valence orbitals spread over the entire molecule, it is reasonable to assume that differences in the initial charge distributions will start to even out quickly. Therefore, dissociation after C 1*s* and S 2*p* ionization events should resemble closely the dissociation after Br 3*d* ionization. As expected, the PIPICO pattern slopes in area I remain the same despite the change in ionization site. The maps for other ionization sites are given in the electronic supplementary information[+].

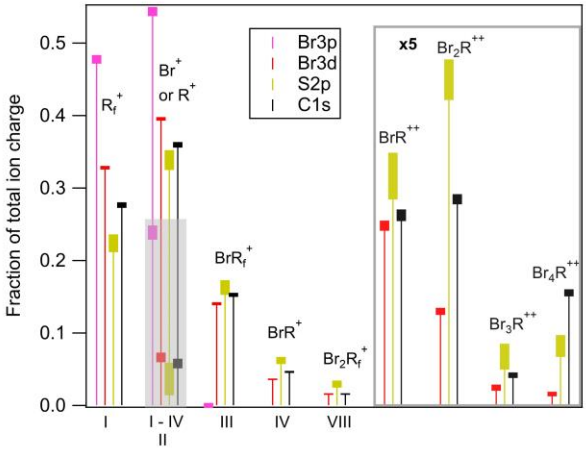


Fig. 9. Fractions of total released charge carried by various singly and doubly (x5 ) charged ions, measured in coincidence with inner-shell photoelectrons from Br, S and C atoms. The lower markers on the ($Br^+$ or $R^+$) ion bar within the gray area denote the estimated fraction of the these ions that come from the ($Br^+$, $R^+$) and ($Br^+$, $Br^+$) dissociation channels (see text for details). Error limits are marked by the thick regions of the bars. Roman numerals under the ion fractions refer to the regions in the PIPICO map (Fig. 3) from which the major contribution of the ions comes from.

Core ionization of deeper orbitals leads to multiple Auger decay steps, in which higher charge states than dications are created as the starting point of dissociation. In the case of different charge states of the parent molecule, the dissociation landscape can be very different. Nevertheless, here we include for comparison also the dissociation processes after Br 3*p* ionization. The Br 3*p* has the vertical binding energy of 196.3 eV for Br $3p_{1/2}$ and 189.6 eV for Br $3p_{3/2}$ as determined in this study. Comparison with the Br 3*d* binding energy of approximately 77 eV shows, that CosterKronig Auger transitions Br $3p^{-1} \rightarrow 3d^{-1}V^{-1}$ are possible. These $3d^{-1}V^{-1}$ states decay further into the $V^{-3}$ states and it is thus expected that the dissociation following the Br 3*p* core ionization is mostly that of trications. Note that although a two-step Auger decay as denoted above is also energetically possible for C $1s^{-1}$ and S $2p^{-1}$ core-hole states, it would require an interaction of core electrons of different atomic sites, which is expected to have a very low probability.

Fig. 9 presents the fraction of the total detected charge in dissociation events following the core ionization of the different atomic sites of Br, C and S. The bar graph shows the average fraction of charge carried by various singly and doubly charged ionic fragments that were already identified in the detailed analysis of the dissociation pattern following the Br 3*d* ionization and Auger decay. The Roman numeral labels link the ions to the ion pair patterns observed in Fig. 3 from which the majority of the detected ionic species originate. The $Br^+(R^+)$ ions warrant a special consideration. Together, they carry the largest fraction of the positive charge in dissociation. As discussed earlier, due to the mass overlap, a reliable separation of the atomic bromine ions and the thiophene ring ions is not possible. A further insight can be obtained, however, by a combination of the coincident ion pair production analysis and the single ion yields, on which Fig. 9 is based.

As was seen in the case of Br 3*d* ionization (and is valid also for the other core-ionization sites), most of the $R_f^+$ ions are produced in coincidence with mass 80u, which therefore must be the $Br^+$ ion. Similarly, the majority of the $BrR_f^+$ and $BrR^+$ ions are in ion pair channels that require a $Br^+$ ion as counterpart. We generated the PIPICO maps for all core-ionization events shown in Fig. 9 and determined the percentages of the $R_f^+$ and $BrR_f^+$ ions that come in coincidence with $Br^+$. For $R_f^+$, the percentages were 66%, 68%, 67% and 73% for the Br 3*p*, Br 3*d*, C 1*s* and S 2*p* ionization events, respectively. For $BrR_f^+$, the percentages were 66%, 59%, 49% and 52% for the Br 3*p*, Br 3*d*, C 1*s* and S 2*p* ionization events, and for $BrR^+$ they were 100%, 88%, 92% and 89%. We removed from the $Br^+$ ion fractions in Fig. 9 the counterpart ions for the $R_f^+$, $BrR_f^+$ and $BrR^+$ fragments,

according to their yields and the percentages of coincidence with $Br^+$. The residual M=80 ion fractions are shown within the gray area of Fig. 9 and they correspond to either ($Br^+$, $Br^+$) or ($R^+$, $Br^+$) dissociation charge separation channels. It should be noted that this fraction is underestimated in our experiment, since in these dissociation channels, the two ions arrive to the detector very close in time, which often results in only one of the ions being detected. However, a comparison between the different ionization sites can still be made also for the ions in this category.

A comparison of the different core-ionization sites and ionized orbitals shows, first, that the Br 3*p* ionization has indeed a very different character. The smaller fragments $R_f^+$ and $Br^+$ (or $R^+$) now carry almost all the released positive charge. They are also the fragments that require the largest amount of internal energy in dicationic dissociation (Fig. 6), which is consistent with a more energetic fragmentation of higher charge states.

The released charge distribution in Fig. 9 between ions is, however, much more similar in the dicationic dissociation after Br 3*d*, C 1*s* and S 2*p* ionization. Amongst the cations, the lightest fragments show the largest differences, with the $R_f^+$ carrying a 46% larger fraction of the total charge following Br 3*d* ionization than following S 2*p* ionization, for example. More striking variations occur, however, amongst the dications. There is about 10 times more stable parent dicationic species following the C 1*s* ionization than after Br 3*d* ionization, and about 5 times more than after S 2*p* ionization. Also, differences in the production of a stable dication after losing two neutral Br atoms (or $Br_2$) are large.

### 4.2 Theoretical predictions of the ionization-site-dependent effects

#### 4.2.1 Population of the final states of the Auger decay

In order to explore whether a qualitative insight into the molecular Auger decay is helpful in interpreting the ionization-sitedependent and internal-energy-dependent changes in the fragmentation pattern, we simulated the electronic structure of the $Br_4R$ molecule in the Kohn–Sham density functional theory (DFT) with the B3LYP[25] exchange-correlation potential. We approximated the Auger final state energies for a vertical transition in the ground state equilibrium geometry without any orbital relaxation. In the spirit of Koopmans' theorem, we use orbital eigenenergies to estimate the energies of the two-hole states, as the additive inverse of the sums of the eigenenergies of the two singly occupied orbitals (denoted *r* and *s*, $r \geq s$) that define the state. We ignore coupling to total spin eigenstates in this calculation, and then model the Auger rates by the locality of the two contributing valence holes at the atomic site of the core-hole orbital *c* by orbital-wise Mulliken analysis[26,27]. In this approximation we obtain relative Auger rates $R_{rs,c}$ as

$$R_{rs,c} \propto \begin{cases} P(r,c), & r = s \\ 2[P(r,c)+P(s,c)], & r > s \end{cases} \qquad (4)$$

where the Mulliken population of orbital *x* at the site of core-hole orbital *c* is denoted by $P(x,c)$. Weight factor 2 and summation in the square brackets are due to combinatorics, as there are four possible spin states with $r > s$ and one for $r = s$. For the calculations we used the cc-pVTZ basis set[28–30] and the PSI4 v.1.3.2 software package[31], using the default options. We implemented the orbital-wise Mulliken population analysis ourselves by using the Python interface of PSI4[32].

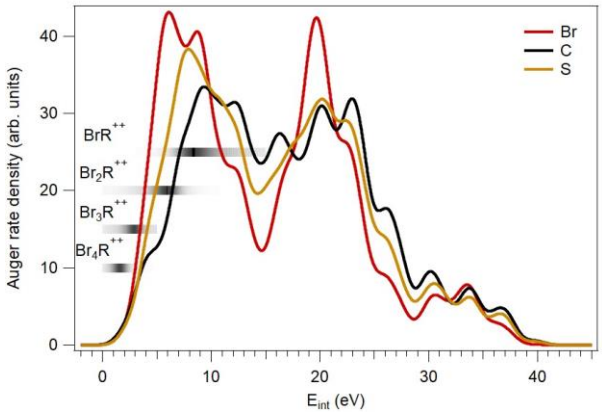


Fig. 10. Simulated population curves of the dicationic states for different core-hole sites of $Br_4R$ as a function of internal energy of the Auger final state relative to $V_{DIP}$. The graphs are normalized to the same area. The final-state energy ranges producing $Br_xR^{++}$ dicationic species are indicated by gray shading.

The approximation stems from the view that Auger processes occur locally due to the localized core-orbital appearing in the related Coulomb integrals. Although the form presented here is not strictly exact even in the Hartree-Fock (HF) theory, it allows for evaluation of estimates using only bound orbitals from a quantum chemistry package. Moreover, using orbital eigenenergies circumvents the more laborious approach of state-wise optimization.

As a result of the aforementioned calculation, the population curve of the Auger final states as a function of energy is obtained as Auger-rate-weighted sum of $\delta$-functions. However, actual transitions to each electronic state span a certain energy range due to accompanying rotational and vibrational excitations. For this reason and for easier comparison with the experiment, the calculated $\delta$-peak spectra were convoluted with a Gaussian of 2 eV FWHM for all three core-hole sites, as shown in Fig. 10. Moreover, the Br and C spectra are superpositions of Auger rate transitions from two inequivalent bromine and carbon core sites. Presented in the internal-energy scale (origin derived as for the experiment), the simulated curves approximate the occupation distributions of the two-hole states without the need to consider possible spinorbit splitting of the intermediate core-ionized state. Similar approaches have been successfully taken elsewhere to simulate Auger spectra[33].

The dicationic state population curves assuming vertical transitions do not explain the drastic differences in the production of parent dication observed in Fig. 9. In the energy region relevant for its production, the core-hole-site-specific population curves do not differ notably.

#### 4.2.2 Molecular dynamics prior to the Auger decay

Since the static model does not explain the differences in dicationic parent survival probabilities, we simulated molecular dynamics during the existence of the various core holes. As there is no literature data for the core-hole lifetimes in tetrabromothiophene, we used the lifetimes determined from other molecules. Although different chemical environments can influence the corehole lifetimes[34,35], these values serve as good approximations for the present purpose. The core-hole lifetime is about 9 fs for both the C 1*s* core hole in $CF_4$ [36] and the S 2*p* core hole in $H_2S$[37]. The Br 3*d* core-hole lifetime is somewhat shorter, about 7 fs in HBr[38]. It should be kept in mind that these values are statistical exponential decay constants, with about two thirds of the core holes decaying before that time has elapsed and a third after, with an occasional much longer survival time.

We carried out *ab initio* molecular dynamics with the Z+1 approximation, where the nuclear charge at the hole site and that of the molecule are both incremented by one elementary unit.[39,40] The approximation accounts for reduced screening of the nucleus while still forcing closed-shell occupation in the molecular valence. As a result, core-ionized-state simulations are transformed to those of the electronic ground state of a modified system. We ran these simulations using the velocity-Verlet algorithm[41] with a time-step of 1 fs for the five symmetrically unique sites of the molecule. The previously described electronic structure method and software implementation were used.

Fig. 11 presents the ensuing molecular dynamics after the core ionization of Br, S and C atoms. The figure shows the changes in the molecular geometry in the core-hole state after 25 fs (chosen to best illustrate the excited normal modes) has elapsed. Ionization and creation of a core hole commonly result in bond length changes, also apparent here (see *e.g.* refs[42,43]). As seen from the two top panels, core ionization of Br initiates quite strong molecular vibrations, which can be described as the C-Br bond stretch. Furthermore, during the timescale determined by the lifetime of 7 fs of the Br 3*d* core hole, the bond is in the extension phase. In the case of C core ionization (the middle panels), the vibrational excitations are the weakest and more uniformly spread across different bonds.

The primary effect of the molecular dynamics in the Br $3d^{-1}$ state is thus adding vibrational energy, concentrated on one C-Br bond that becomes stretched. As seen from the earlier analysis, the dissociation of tetrabromothiophene has a strong tendency to start with the separation of neutral bromine(s). The intact parent dication is produced only when the molecule is in a very low internal energy state (most likely $HOMO^{-2}$). Therefore, any additional energy that was converted into nuclear potential energy prior to the Auger could then have a dramatic impact on the survival probability of the parent dication, as it is a relatively rare and sensitive event. In the case of Br core ionization, concentrating (even a small amount of) additional energy into stretching the CBr bonds will weaken that bond sufficiently so that it will almost certainly dissociate after the Auger decay takes place. On the other hand, the vibrational excitations after the C 1*s* ionization are considerably weaker and they do not affect the C-Br bonds significantly, therefore the core-hole state's molecular dynamics has much less effect on the eventual dissociation in terms of the parent survival probability. S 2*p* ionization is a case in between, where the molecular dynamics in the core-hole state does affect two C-Br bonds, mostly as a bending type excitation.

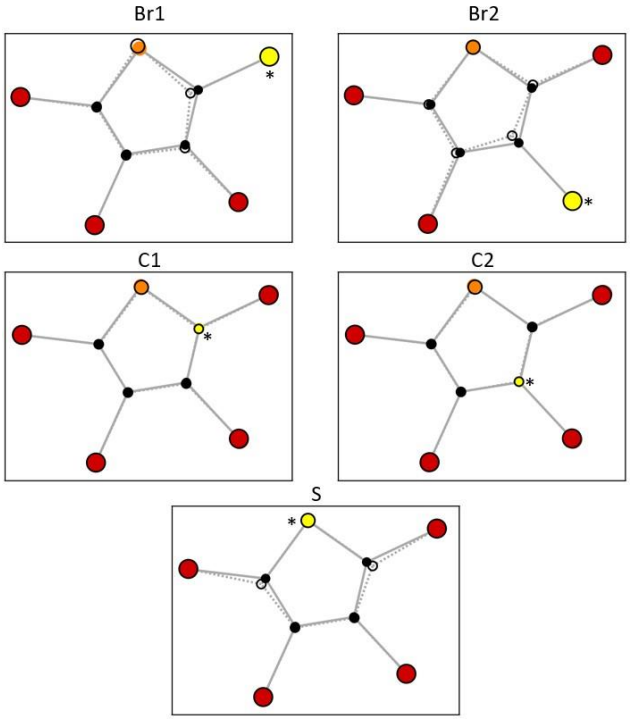


Fig. 11. Molecular dynamics in the symmetrically unique core-hole states. The atom with the core hole, modeled according to the Z+1 model, is marked as yellow and with an asterisk. The ground-state equilibrium geometry is shown by colored markers and solid lines, the geometry after 25 fs of the core-hole creation is shown by empty circles and dashed bond lines.

The above explanation is supported by Fig. 12, which shows the change in dicationic ground state's energy along the coreionized molecular trajectories. The figure shows that the molecular dynamics relaxing the *core-ionized* state energy would lead to geometries with higher *dicationic* ground state energies. This is the case especially for the Br and S core ionization, whereas for C hole-states the effect is small. For the majority of core hole instances, the energy increase will be less than at the lifetime point of the corresponding core ionization, marked in Fig. 12, but occasionally it can be much larger. Thus, the molecular dynamics in the Br 3*d* and S 2*p* core-hole states would result in Auger decay populating a higher-lying portion of the dicationic ground state's ($HOMO^{-2}$) potential energy surface, as compared to the transitions in the neutral ground state geometry. The effect is much less for the C 1*s* core hole. The ensuing molecular dynamics on the $HOMO^{-2}$ potential energy surface after the Auger transition from the Br $3d^{-1}$ state, and also from the S $2p^{-1}$ state, has more energy available for dissociation, offering a qualitative explanation for the observed relative yield differences of the parent dications.

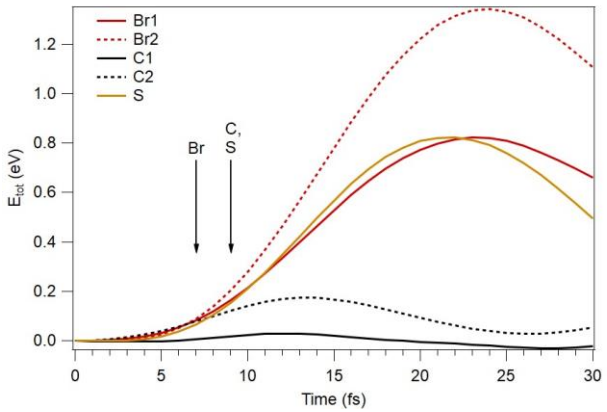


Fig. 12. Dicationic ground state energy after molecular dynamics in a core-hole state and Auger decay, with zero corresponding to the energy in the initial neutral ground state geometry. The arrows mark the core-hole lifetimes.

## 5 Conclusion

Based on internal-energy-resolved multiparticle coincidence experiments and PIPICO slope analysis, dicationic tetrabromothiophene dissociates primarily sequentially. Dissociation generally starts with neutral Br loss, which is followed by deferred charge separation. One or both of the released cationic fragments may still undergo secondary dissociation. Based on the observations, the most important fragmentation pathways are presented in the dissociation tree model.

For low-energy dicationic states, stable parent molecule can also be observed, or the dissociation can stop after the neutral Br separation stage with $Br_nR^{++}$, $n$=1-3 fragments. Intact thiophene ring fragment $C_4S^+$ was observed, but ring break-up is prevalent upon core ionization. PIPICO slope analysis suggests that the ring break-up can occur already in the first, neutral Br separation stage, *i.e.* the ejected Br atoms "rip apart" the thiophene ring, with carbon atoms remaining attached to Br. When large amounts of internal energy is available, the prevalent end products of dissociation are the ring fragments, especially $S^+$,$C_3^+$ and $CS^+$, and the $Br^+$ ion from the bromine that remained attached to that fraction of the ring in the first stage.

While the sequential model appears to fit with the observations remarkably well, properly accounting for the momentum correlations, it cannot be strictly confirmed. Alternatively the dissociation tree could accidentally describe increasingly complete fragmentation with increasing energy; in such a case the various stages could overlap in time. In this regard, tetrabromothiophene and similar halogenated cyclic molecules offer a promising target for femtosecond-scale time-resolved studies. Especially in the case of full halogenization, there will be no ultrafast hydrogen motion, and dissociation dynamics will therefore be feasible for current free electron laser experiments to temporarily resolve.

The overall fragmentation landscape and fragment yields were found to be dependent on the initial atomic site of core ionization, although the effects are, in general, minor. The strongest influence was found in the yields of dications – fragments with neutral Br loss and, in particular, the intact parent molecule. A theoretical investigation of the population of the various dicationic electronic states by the Auger decay of the various core holes did not offer a clear explanation of the observed site dependencies. However, taking into account the short period of molecular dynamics while the molecule is in the core-hole state suggested a reason for the major changes in the intact parent survivability after the Auger decay. Molecular dynamics simulations showed that, particularly in the Br $3d^{-1}$ state, strong vibrational excitations involving the Br-C bond were induced, and that the resulting changes in the geometry within the core-hole lifetime would populate less stable regions of lowest dicationic state's potential energy surface. Thus, even in a molecule with no hydrogen and ultrafast molecular dynamics, our results suggest that the nuclear relaxation in the core-hole state could play a key role in specific aspects of the eventual molecular dissociation.

## Conflicts of interest

There are no conflicts to declare.

## Acknowledgements

LP acknowledges financial support from The Vilho, Yrjö and Kalle Väisälä Foundation of the Finnish Academy of Science and Letters. JN acknowledges Academy of Finland for funding via project 331234. SM acknowledges financial support from Knut and Alice Wallenberg Foundation and the COST Action CA18212 - Molecular Dynamics in the GAS phase (MD-GAS), supported by COST (European Cooperation in Science and Technology). EK acknowledges funding by the Academy of Finland.

We acknowledge MAX IV Laboratory for time on Beamline FinEstBeAMS under proposal 20190446. Research conducted at MAX IV, a Swedish national user facility, is supported by the Swedish Research council under contract 2018-07152, the Swedish Governmental Agency for Innovation Systems under contract 2018-04969, and Formas under contract 2019-02496.

## References

1 E. Itälä, D. T. Ha, K. Kooser, E. Rachlew, M. A. Huels and E. Kukk, *The Journal of Chemical Physics*, 2010, **133**, 154316.

2 M. Kawade, A. Saha, H. P. Upadhyaya, A. Kumar, P. D. Naik and P. Bajaj, *The Journal of Physical Chemistry A*, 2012, **116**, 10656–10667.

3 B. Erk, R. Boll, S. Trippel, D. Anielski, L. Foucar, B. Rudek, S. W. Epp, R. Coffee, S. Carron, S. Schorb and et al., *Science*, 2014, **345**, 288–291.

4 K. Motomura, E. Kukk, H. Fukuzawa, S.-I. Wada, K. Nagaya, S. Ohmura, S. Mondal, T. Tachibana, Y. Ito, R. Koga and et al., *The Journal of Physical Chemistry Letters*, 2015, **6**, 2944–2949.

5 P. Bolognesi, J. A. Kettunen, A. Cartoni, R. Richter, S. Tosic, S. Maclot, P. Rousseau, R. Delaunay and L. Avaldi, *Phys. Chem. Chem. Phys.*, 2015, **17**, 24063–24069.

6 R. Boll, B. Erk, R. Coffee, S. Trippel, T. Kierspel, C. Bomme, J. D. Bozek, M. Burkett, S. Carron, K. R. Ferguson and et al., *Structural Dynamics*, 2016, **3**, 043207.

7 K. Nagaya, K. Motomura, E. Kukk, H. Fukuzawa, S. Wada, T. Tachibana, Y. Ito, S. Mondal, T. Sakai, K. Matsunami and et al., *Physical Review X*, 2016, **6**, 021035.

8 T. Takanashi, K. Nakamura, E. Kukk, K. Motomura, H. Fukuzawa, K. Nagaya, S.-i. Wada, Y. Kumagai, D. Iablonskyi, and Y. Ito, et al., *Phys. Chem. Chem. Phys.*, 2017, **19**, 19707–19721.

9 M. Burt, R. Boll, J. W. L. Lee, K. Amini, H. Köckert, C. Vallance, A. S. Gentleman, S. R. Mackenzie, S. Bari, C. Bomme and et al., *Physical Review A*, 2017, **96**, 043415.

10 A. Rudenko, L. Inhester, K. Hanasaki, X. Li, S. J. Robatjazi, B. Erk, R. Boll, K. Toyota, Y. Hao, O. Vendrell and et al., *Nature*, 2017, **546**, 129–132.

11 K. Amini, E. Savelyev, F. Braußе, N. Berrah, C. Bomme, M. Brouard, M. Burt, L. Christensen, S. Düsterer, B. Erk and et al., *Structural Dynamics*, 2018, **5**, 014301.

12 H. P. Upadhyaya, *Rapid Communications in Mass Spectrometry*, 2019, **33**, 1598–1612.

13 E. Kukk, H. Myllynen, K. Nagaya, S. Wada, J. D. Bozek, T. Takanashi, D. You, A. Niozu, K. Kooser, T. Gaumnitz and et al., *Physical Review A*, 2019, **99**, 023411.

14 Y.-C. Cheng, B. Oostenrijk, J. Lahl, S. Maclot, S. Augustin, G. Schmid, K. Schnorr, S. Meister, D. Rompotis, B. Manschwetus *et al.*, *Journal of Physics B: Atomic, Molecular and Optical Physics*, 2021, **54**, 014001.

15 B. A. Kihlman, *Hereditas*, 1963, **49**, 353–370.

16 K. Kobayashi, N. Usami, E. Porcel, S. Lacombe and C. Le Sech, *Mutation Research/Reviews in Mutation Research*, 2010, **704**, 123–131.

17 Y. Duo, Y. Huang, W. Liang, R. Yuan, Y. Li, T. Chen and H. Zhang, *Advanced Functional Materials*, 2020, **30**, 1906010.

18 R. Pärna, R. Sankari, E. Kukk, E. Nõmmiste, M. Valden, M. Lastusaari,K. Kooser, K. Kokko, M. Hirsimäki, S. Urpelainen, P. Turunen, A. Kivimäki, V. Pankratov, L. Reisberg, F. Hennies, H. Tarawneh, R. Nyholm and M. Huttula, *Nuclear Instruments and Methods in Physics Research Section A: Accelerators, Spectrometers, Detectors and Associated Equipment*, 2017, **859**, 83–89.

19 K. Kooser, A. Kivimäki, P. Turunen, R. Pärna, L. Reisberg, M. Kirm, M. Valden, M. Huttula and E. Kukk, *J Synchrotron Rad*, 2020, **27**, 1080–1091.

20 W. C. Wiley and I. H. McLaren, *Review of Scientific Instruments*, 1955, **26**, 1150–1157.

21 G. Prümper and K. Ueda, *Nuclear Instruments and Methods in Physics Research Section A: Accelerators, Spectrometers, Detectors and Associated Equipment*, 2007, **574**, 350–362.

22 P. Bolognesi, A. R. Casavola, A. Cartoni, R. Richter, P. Markus, S. Borocci, J. Chiarinelli, S. Toši´c, H. Sa'Adeh, M. Masi˘c and et al., *The Journal of Chemical Physics*, 2016, **145**, 191102.

23 E. Itälä, J. Niskanen, L. Pihlava and E. Kukk, *The Journal of Physical Chemistry A*, 2020, **124**, 5555–5562.

24 E. Kukk, D. T. Ha, Y. Wang, D. G. Piekarski, S. Diaz-Tendero, K. Kooser, E. Itälä, H. Levola, M. Alcamí, E. Rachlew and F. Martín, *Phys. Rev. A*, 2015, **91**, 043417.

25 P. J. Stephens, F. J. Devlin, C. F. Chabalowski and M. J. Frisch, *The Journal of physical chemistry*, 1994, **98**, 11623–11627.

26 R. S. Mulliken, *The Journal of Chemical Physics*, 1955, **23**, 1833–1840.

27 R. S. Mulliken, *The Journal of Chemical Physics*, 1955, **23**, 1841–1846.

28 T. H. Dunning, *The Journal of Chemical Physics*, 1989, **90**, 1007–1023.

29 D. E. Woon and T. H. Dunning, *The Journal of Chemical Physics*, 1993, **98**, 1358–1371.

30 A. K. Wilson, D. E. Woon, K. A. Peterson and T. H. Dunning, *The Journal of Chemical Physics*, 1999, **110**, 7667–7676.

31 R. M. Parrish, L. A. Burns, D. G. A. Smith, A. C. Simmonett, A. E. DePrince III, E. G. Hohenstein, U. Bozkaya, A. Y. Sokolov,R. D. Remigio, R. M. Richard, J. F. Gonthier, A. James, H. R. McAlexander, A. Kumar, M. Saitow, X. Wang, B. P. Pritchard, P. Verma, H. F. S. III, K. Patkowski, R. A. King, E. F. Valeev, F. A. Evangelista, J. M. Turney, T. D.Crawford and C. D. Sherrill, *J. Chem. Theory Comput.*, 2017, **13**, 3185–3197.

32 D. G. A. Smith, L. A. Burns, D. A. Sirianni, D. R. Nascimento, A. Kumar, A. M. James, J. B. Schriber, T. Zhang, B. Zhang, A. S. Abbott and et al., *Journal of Chemical Theory and Computation*, 2018, **14**, 3504–3511.

33 L. Storchi, F. Tarantelli, S. Veronesi, P. Bolognesi, E. Fainelli and L. Avaldi, *The Journal of chemical physics*, 2008, **129 15**, 154309.

34 R. W. Shaw and T. D. Thomas, *Phys. Rev. Lett.*, 1972, **29**, 689– 692.

35 K. Prince, M. Vondrácek, J. Karvonen, M. Coreno, R. Camilloni, L. Avaldi and M. De Simone, *Journal of Electron Spectroscopy and Related Phenomena*, 1999, **101-103**, 141–147.

36 C. Nicolas and C. Miron, *Journal of Electron Spectroscopy and Related Phenomena*, 2012, **185**, 267–272.

37 S. Svensson, A. Ausmees, S. Osborne, G. Bray, F. Gel'mukhanov, H. Ågren, A. N. de Brito, O.-P. Sairanen, A. Kivimäki, E. Nõmmiste *et al.*, *Physical Review Letters*, 1994, **72**, 3021.

38 P. Lablanquie, H. Iwayama, F. Penent, K. Soejima and E. Shigemasa, *Journal of Electron Spectroscopy and Related Phenomena*, 2014, **195**, 96–100.

39 J. D. Dow, D. Franceschetti, P. Gibbons and S. Schnatterly, *Journal of Physics F: Metal Physics*, 1975, **5**, L211. 40 M. M. Disko, J. C. H. Spence, O. F. Sankey and D. Saldin, *Physical Review B*, 1986, **33**, 5642–5651.

41 W. C. Swope, H. C. Andersen, P. H. Berens and K. R. Wilson, *The Journal of Chemical Physics*, 1982, **76**, 637–649.

42 C. M. Humphries, A. D. Walsh and P. A. Warsop, *Transactions of the Faraday Society*, 1967, **63**, 513.

43 O. Goscinski and A. Palma, *Chemical Physics Letters*, 1977, **47**, 322–326.